Charged-Particle Probing of X-ray Driven Inertial-Fusion Implosions

C. K. Li, *et al.*

Science **327**, 1231 (2010);
DOI: 10.1126/science.1185747

This copy is for your personal, non-commercial use only.

If you wish to distribute this article to others, you can order high-quality copies for your colleagues, clients, or customers by clicking here.

Permission to republish or repurpose articles or portions of articles can be obtained by following the guidelines here.

The following resources related to this article are available online at www.sciencemag.org (this information is current as of March 4, 2010):

Updated information and services, including high-resolution figures, can be found in the online version of this article at:
http://www.sciencemag.org/cgi/content/full/327/5970/1231

This article **cites 18 articles**, 2 of which can be accessed for free:
http://www.sciencemag.org/cgi/content/full/327/5970/1231#otherarticles

This article has been **cited by** 1 articles hosted by HighWire Press; see:
http://www.sciencemag.org/cgi/content/full/327/5970/1231#otherarticles

This article appears in the following **subject collections**:
Physics
http://www.sciencemag.org/cgi/collection/physics

Science (print ISSN 0036-8075; online ISSN 1095-9203) is published weekly, except the last week in December, by the American Association for the Advancement of Science, 1200 New York Avenue NW, Washington, DC 20005. Copyright 2010 by the American Association for the Advancement of Science; all rights reserved. The title *Science* is a registered trademark of AAAS.

shifts, that is, $P_2/P_0 = 0.02$ at $\Delta\lambda = 1.7$ Å. For all cases, we find $P_4/P_0 = 0.09 \pm 0.02$ (here, $P_0 = 50$ μm denotes the radius of the imploded core).

We have achieved symmetric implosions and adequate equatorial x-ray drive without changing the initial inner- and outer-cone laser powers. This tuning mechanism takes advantage of the multiple laser beam interactions (*30*, *31*) with the plasma in the LEH area where all the beams cross. Transferring power into the inner beams allows us to compensate for SRS losses of the inner beams. Although inner beam SRS energy losses of 5 to 7% are energetically small and do not substantially affect radiation temperatures, these losses may affect the local soft x-ray production.

As shown in the inset of Fig. 1, and as indicated by the interference fringes, the crossing lasers in the LEH produce spatial intensity modulations. These intensity modulations further drive plasma electron density modulations that are caused by the ponderomotive force. If these modulations move with the plasma sound speed C_S (in the frame of the plasma), then modulations and laser scattering will grow to large levels, and efficient energy transfer between beams will occur. In the rest frame, the power transfer rate Q is determined by

$$Q \sim [(\omega_1 - \omega_2) - k_A(C_S - V) + i\nu]^{-2} \qquad (2)$$

In Eq. 2, V is the plasma flow velocity, $i\nu$ is the Landau damping rate for acoustic fluctuations, and k_A is the wave number. The frequency detuning between pairs of beams is denoted as $\omega_1 - \omega_2$. This factor allows us to control the energy transfer between cones of beams in integrated hohlraum experiments, and it can be set to transfer power into either cone of beams. Proper choice of the laser wavelengths is therefore required to obtain the desired x-ray drive symmetry.

P_2/P_0 depends linearly on the wavelength tuning difference $\Delta\lambda$ (Fig. 3). This fact has allowed us to tune the implosion symmetry in three shots. This observation has been expected for the small tuning range (*18*, *19*) and constant SRS levels in this study. A linear scaling further agrees with power-transfer calculations that include the detailed calculated plasma conditions and flow profiles in the LEH region. Although the experimental scaling is reproduced, the P_2 zero crossing is not accurately calculated. A difference of 0.5 Å can be explained by, for example, errors of ~10% in the calculated plasma flow.

Moreover, best agreement is observed when including a model that assumes enhanced inner laser beam absorption in the hohlraum gas fill plasma. This assumption is motivated by observations of increasing levels of hot electrons at the peak of the laser drive with increasing wavelength shift. The hot electron fraction reaches levels between 1 and 2% of the laser energy, indicating finite levels of reabsorbed SRS in the hohlraum. Without the absorption model, the calculated slope increases by 20%.

The demonstration of efficient laser coupling and symmetric capsule implosions in cryogenic hohlraum experiments on the NIF meet simultaneous requirements for laser coupling and symmetry for future ignition shots. The measured insensitivity of SRS losses to the power level of the inner cone beams will motivate future higher–radiation-temperature experiments with higher laser intensities and energies.

References and Notes

1. E. Moses, C. R. Wuest, *Sci. Tech. (Paris)* **47**, 314 (2005).
2. C. A. Haynam *et al.*, *Appl. Opt.* **46**, 3276 (2007).
3. D. Clery, *Science* **324**, 326 (2009).
4. J. Nuckolls, L. Wood, A. Thiessen, G. Zimmerman, *Nature* **239**, 139 (1972).
5. R. P. Drake, *High-Energy-Density Physics* (Springer, New York, 2006).
6. B. A. Remington, R. P. Drake, D. D. Ryutov, *Rev. Mod. Phys.* **78**, 755 (2006).
7. R. A. García *et al.*, *Science* **316**, 1591 (2007).
8. D. O. Gough *et al.*, *Science* **272**, 1296 (1996).
9. J. D. Lindl *et al.*, *Phys. Plasmas* **11**, 339 (2004).
10. S. Atzeni, J. Meyer-ter-Vehn, *The Physics of Inertial Fusion* (Oxford Univ. Press, New York, 2004).
11. R. L. McCrory *et al.*, *Phys. Plasmas* **15**, 055503 (2008).
12. L. J. Suter *et al.*, *Phys. Rev. Lett.* **73**, 2328 (1994).
13. R. L. Kauffman *et al.*, *Phys. Rev. Lett.* **73**, 2320 (1994).
14. W. J. Krauser *et al.*, *Phys. Plasmas* **3**, 2084 (1996).
15. S. H. Glenzer *et al.*, *Phys. Rev. Lett.* **80**, 2845 (1998).
16. W. L. Kruer, S. C. Wilks, B. B. Afeyan, R. K. Kirkwood, *Phys. Plasmas* **3**, 382 (1996).
17. W. L. Kruer, *The Physics of Laser Plasma Interactions* (Addison-Wesley, New York, 1988).
18. P. Michel *et al.*, *Phys. Rev. Lett.* **102**, 025004 (2009).
19. P. Michel *et al.*, *Phys. Plasmas* **16**, 042702 (2009).
20. B. J. MacGowan *et al.*, *Phys. Plasmas* **3**, 2029 (1996).
21. J. C. Fernandez *et al.*, *Phys. Plasmas* **4**, 1849 (1997).
22. G. B. Zimmerman, W. L. Kruer, *Plasma Phys. Contr. Fusion* **2**, 85 (1975).
23. R. L. Berger, C. H. Still, E. A. Williams, A. B. Langdon, *Phys. Plasmas* **5**, 4337 (1998).
24. D. H. Froula *et al.*, *Rev. Sci. Instrum.* **75**, 4168 (2004).
25. A. J. Mackinnon *et al.*, *Rev. Sci. Instrum.* **75**, 4183 (2004).
26. E. L. Dewald *et al.*, *Rev. Sci. Instrum.* **75**, 3759 (2004).
27. J. A. Oertel *et al, Rev. Sci. Instrum*. **77**, 10E308 (2006).
28. A. A. Hauer *et al.*, *Phys. Plasmas* **2**, 2488 (1995).
29. O. L. Landen *et al.*, *Phys. Plasmas* **6**, 2137 (1999).
30. K. B. Wharton *et al.*, *Phys. Rev. Lett.* **81**, 2248 (1998).
31. R. K. Kirkwood *et al.*, *Phys. Rev. Lett.* **89**, 215003 (2002).

32. This work was performed under the auspices of the U.S. Department of Energy by Lawrence Livermore National Laboratory under contract DE-AC52-07NA27344.

7 December 2009; accepted 15 January 2010
Published online 28 January 2010;
10.1126/science.1185634
Include this information when citing this paper.

Charged-Particle Probing of X-ray–Driven Inertial-Fusion Implosions

C. K. Li,[1]* F. H. Séguin,[1] J. A. Frenje,[1] M. Rosenberg,[1] R. D. Petrasso,[1] P. A. Amendt,[2] J. A. Koch,[2] O. L. Landen,[2] H. S. Park,[2] H. F. Robey,[2] R. P. J. Town,[2] A. Casner,[3] F. Philippe,[3] R. Betti,[4] J. P. Knauer,[4] D. D. Meyerhofer,[4] C. A. Back,[5] J. D. Kilkenny,[5] A. Nikroo[5]

Measurements of x-ray–driven implosions with charged particles have resulted in the quantitative characterization of critical aspects of indirect-drive inertial fusion. Three types of spontaneous electric fields differing in strength by two orders of magnitude, the largest being nearly one-tenth of the Bohr field, were discovered with time-gated proton radiographic imaging and spectrally resolved proton self-emission. The views of the spatial structure and temporal evolution of both the laser drive in a hohlraum and implosion properties provide essential insight into, and modeling validation of, x-ray–driven implosions.

Understanding and characterizing x-ray drive and capsule implosions is critical to indirect-drive inertial confinement fusion (ICF) (*1*–*3*), a primary approach to achieving nuclear fusion ignition at the National Ignition Facility (NIF). Properties of the x-ray drive are also of fundamental scientific importance for a wide range of basic and applied high-energy-density physics (HEDP), including laboratory astrophysics, space physics, and materials sciences (*4*, *5*). Conventionally, diagnosing drive and implosions in these experiments has relied on techniques using x-rays, ultraviolet or visible light, and fusion neutrons. Although they have inherent sensitivity to both plasma density and field structures (*6*–*9*), charged particles have not previously been used because of practical limitations and challenging complexities.

We present experiments using monoenergetic proton radiography (*10*) and charged-particle spectroscopy (*11*) to study the x-ray drive and capsule implosions in gold (Au) hohlraums [a hohlraum is an enclosure that creates an environment filled with a nearly blackbody (Planckian) radiation field when it is irradiated by high-power lasers (*2*, *3*)].

---

[1] Plasma Science and Fusion Center, Massachusetts Institute of Technology, Cambridge, MA 02139, USA. [2] Lawrence Livermore National Laboratory, Livermore, CA 94550, USA. [3] CEA, DAM, DIF, F-91297 Arpajon, France. [4] Laboratory for Laser Energetics, University of Rochester, Rochester, NY 14623, USA. [5] General Atomics, San Diego, CA 92186, USA.

*To whom correspondence should be addressed. E-mail: ckli@mit.edu

These measurements have allowed a number of important phenomena to be observed. In particular, three types of spontaneous electric (E) fields, differing by two orders of magnitude in strength with the largest approaching the Bohr field ($= ea_0^{-2} \sim 5 \times 10^{11}$ V m^{-1}, where a_0 is the Bohr radius), were observed at different locations (in or outside the hohlraums, and inside the imploded capsules). The experiments demonstrate the absence of stochastic filamentary patterns and striations generally found in laser-driven implosions (*6*). We also observed plasma flow, supersonic jet formation, and self-generated magnetic (B) fields (*12*, *13*); determined the areal density (ρR) and implosion symmetry; and sampled different implosion phases.

The experiments were performed at the OMEGA laser facility (*14*). In the backlighting experiment (Fig. 1A) the hohlraum had a 2.4-mm diameter, 3.8-mm length, and 100% laser-entrance holes (LEH, defined as the ratio of hole size to hohlraum diameter) with a 25-μm-thick Au wall over-coated on the inside with 0.3 μm parylene (CH) liner to effectively impede and tamp the flow of Au plasma off the wall. The hohlraum was driven by 30 laser beams with wavelength 0.351 μm and total laser energy ~11 kJ in a 1-ns square pulse. The laser beams had full spatial and temporal smoothing (*15*), and phase plates SG4 (super Gaussian with power of 4) were used. The capsule was a 30-μm-thick plastic shell of diameter 550 μm filled with 50 atm H_2 or D_2 gas. The designed radiation temperatures (~150 eV) and consequent capsule compression (≈10) were low. The backlighter was a D^3He-gas–filled, glass-shell capsule with a 420-μm diameter and a 2-μm shell thickness, imploded by 30 laser beams. Two types of fusion protons with discrete birth energies of 14.7 and 3.0 MeV are produced in nuclear fusion reactions ($D + {}^3He \rightarrow \alpha + p$ and $D + D \rightarrow T + p$) ~80 ps (the nuclear burn duration). The images were recorded by CR-39 track detectors, and the timing of the proton sampling (i.e., the time when backlighting protons starting to pass through the subject target) was adjustable (*6*–*10*).

Radiographs made by 15-MeV D^3He protons (*16*) covering a typical ICF implosion sequence (Fig. 1) contain both spatial and energy information because the CR-39 detector records the position and energy of each individual proton (*6*–*10*). The images are displayed to show either proton fluence versus position (Fig. 1B) or proton mean energy versus position (Fig. 1C), to provide time-dependent information about field distributions, capsule compression, and hohlraum plasma conditions.

A striking feature shown in both fluence (Fig. 1B) and energy images (Fig. 1C) is a five-pronged, asterisk-like pattern surrounding the imploding capsule, a consequence of the laser beam positions on the hohlraum wall. To explore this structure, a solid CH sphere driven with identical conditions was imploded (Fig. 2). This solid sphere would not implode (*3*), in contrast to the example in Fig. 1. The plasma conditions and five-pronged asterisk-like structure inside the hohlraums remain nearly identical. Figure 2A shows the simulation of the laser intensity distribution associated with the OMEGA 58.8°- and 42.0°-beam configurations [the locations of the laser beams are illustrated in the simulation (Fig. 1A)], viewed from a location just outside the LEH. The ten 58.8° laser beams are grouped to form five pairs. An azimuthal lineout of the fluence image (Fig. 2B) indicates that the asterisk spokes are formed between two expanding plasma bubbles that are generated by "nearest neighbor" (58.8°) laser beam pairs (illustrated in Fig. 2A), whereas the periodic patterns (narrow fingers) between these spokes are associated with the remaining laser beam distributions.

For a physical picture of the formation of the asterisk spokes, the expanding plasma bubbles [electron temperature $T_e \sim 1$ keV, ion temperature $T_i \sim 10$ eV, and electron density n_e (in units of critical electron density at 0.35 μm) $\sim 0.1 n_c$] (*9*) generated on the hohlraum wall near the laser spots are governed by plasma hydrodynamics because the plasma thermal pressure is much larger than the magnetic pressure. Their hydrodynamic expansion is scaled by the sound speeds [$C_s \sim (ZT_e m_i^{-1})^{1/2} \sim 250$ μm ns^{-1} for CH and ~150 μm ns^{-1} for Au, where Z is the average ion charge state]. For an adiabatic rarefaction expansion of an ideal gas, the expansion speed is 3 C_s, close to the observed jet speed (~4 C_s). Furthermore, the hot electrons advancing ahead of the rarefaction expansion due to their high mobility may further boost the motion of leading-edge CH and Au ions ablating off the hohlraum wall by an additional sound speed (~C_s) factor (*9*). With ~200 μm between pairs of bubbles (Fig. 2A), it is observed that adjacent CH bubbles coalesce in ~0.1 ns and reach the hohlraum axis in ~1 ns, with the Au plasma bubble trailing behind (Fig. 2C).

To identify potential mechanisms for generating the spoke-like structure, we consider whether the image features seen in the region between the capsule and the hohlraum wall are due to collisional scattering in the plasma or to proton deflections by E or B fields. This analysis is helped by the fact that nearly simultaneous images are recorded with two different but very accurately known proton energies. For collisional scattering in matter, deflection angles vary inversely with the proton energy ($\theta \propto \varepsilon_p^{-1}$) (*17*). For B fields, it follows from the Lorentz force law that the deflection angles are inversely proportional to the square root of the proton energy ($\theta \propto \varepsilon_p^{-1/2}$) (*17*), whereas those due to E are inversely proportional to the proton energy ($\theta \propto \varepsilon_p^{-1}$) (*17*). The energy scaling due to B is unique, whereas that due to E and collisional scattering is degenerate. Deflections due to collisional scattering are accompanied by an energy loss, whereas those due to transverse E fields are not. Thus, discrimination between the two effects is possible.

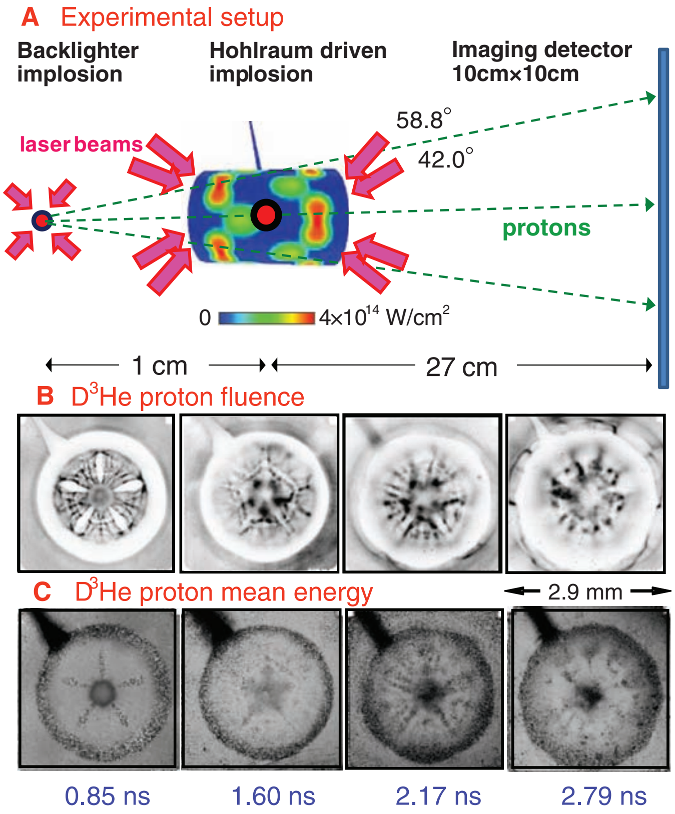

Fig. 1. (**A**) Schematic of the experimental setup, with proton backlighter, hohlraum-driven implosion, CR-39 imaging detector, and laser drive beams. Fifteen laser beams entered each end of the hohlraum: 5 with incident angle 42° and 10 with angle 58.8°. The colors shown on the hohlraum wall indicate the laser intensity distribution [modeled by VISRAD (*26*)]. The proton backlighter was driven by 30 laser beams with total laser energy ~11 kJ in a 1-ns square pulse. The 15 MeV D^3He backlighting protons (*16*) passed through the laser-driven hohlraum, sampling plasma conditions, and capsule implosions at different times. Images in (**B**) show proton fluence (within each image, darker means higher fluence), whereas images in (**C**) show proton energy (within each image, darker means more proton energy loss and therefore more matter traversed). The gray-scale mapping for image display is different in each image. The hohlraum-mounting stalk appears in the upper left corner of each image.

The *B* field can be excluded by symmetry. The five-pronged asterisk-like pattern in Figs. 1 and 2 provides a constraint that rules out the possibility of self-generated *B* fields as a major cause for the formation of this structure, because the toroidal *B*-field topology around the laser spots or radial jets cannot result in azimuthal proton deflections.

With the *B* field excluded, the other two possible mechanisms for deflecting the proton trajectories are intense, local *E* fields associated with strong azimuthally oriented electron pressure gradients (∇p_e) in the spokes, and proton collisional scattering in the spokes.

The possibility that the proton deflection is mostly caused by collisional scattering that deflects protons out of the dense spoke can be ruled out through the measurements of the proton energy loss. It can be shown (Fig. 1C, $t = 0.85$ ns) that there is little energy loss for protons passing through the major spokes. In the regions between the five spokes (Figs. 1C and 2D), there are high-contrast features in the fluence image, including the counterparts of the spokes generated by the "far" beams on the other side of the hohlraum, but very little variation in energy (Fig. 1C) (*18*).

This leaves the electric fields as the remaining cause. Using the spoke widths estimated in the images, the spreading of 15 MeV proton $\delta_{15} \sim 90$ μm (*18*), $\int \mathbf{E} \times d\ell \sim 3 \times 10^5$ V (where $d\ell$ is the differential path length along the proton trajectory through the field area). Taking a scale length ~1 mm (the size of laser spot) for field in a jet-spoke results in $E \sim 3 \times 10^8$ V m^{-1} with field directions pointed away from the spoke. This is the first time such strong, local *E* fields inside the hohlraum have been inferred even though the cavity is effectively a Faraday cage (*9*). The effects of such fields can affect important physics issues, including laser-plasma instabilities, modification of the plasma electron distribution, and implosion symmetry.

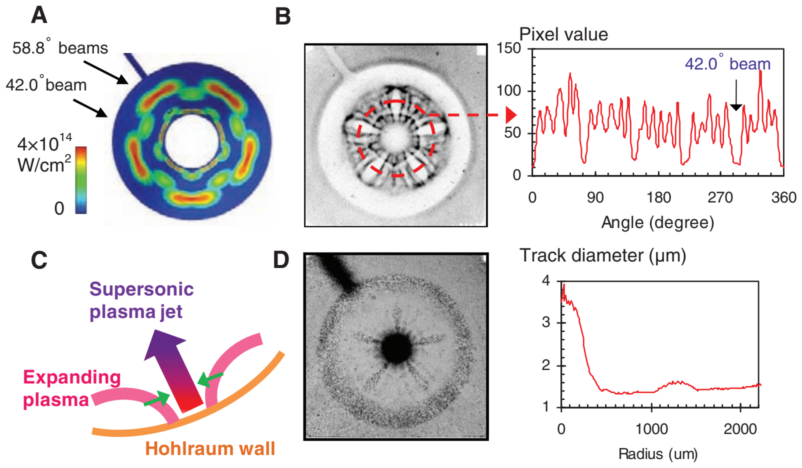

Fig. 2. (**A**) The laser intensity distribution associated with the OMEGA 58.8°-beam and 42°-beam configurations, viewed just outside of the LEH, and modeled by VISRAD. (**B**) An azimuthal lineout of the asterisk fluence image indicates that the periodic pattern is associated with the "near" and "far" laser beam distributions (relative to the detector). (**C**) A cartoon illustrating the formation of a supersonic, radially directed plasma jet as the two laser-driven expanding plasma bubbles approach one another. (**D**) Radial lineout of track diameter from the proton energy image, which indicates the energy-loss-implied areal densities for backlighting protons passing between the hohlraum and the capsule (solid sphere).

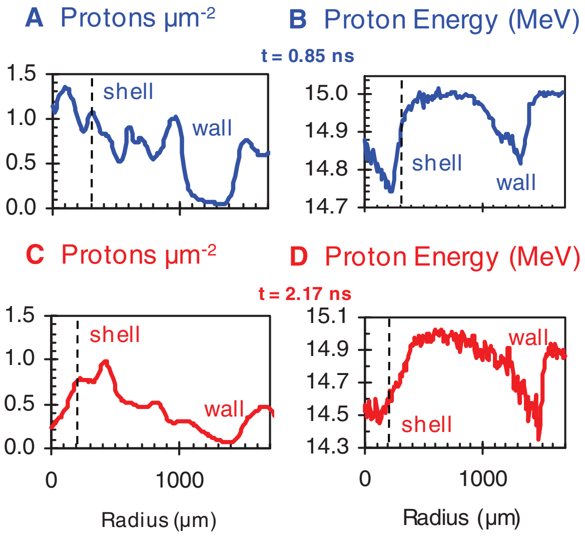

Fig. 3. Radial profiles of proton fluence images and energy images at $t = 0.85$ ns [blue color, (**A**) and (**B**)], and at 2.17 ns [red color, (**C**) and (**D**)] from Fig. 1, B and C, respectively. The profiles are averaged over azimuthal angle, excluding the stalk region. The dashed lines indicate the positions of the outer shells. The difference in fluence levels outside the two capsules is due to the difference in the backlighter proton yields.

Another feature in Fig. 1B of note is that a fluence peak occurs in the capsule center during the early stages of the implosion ($t = 0.85$ ns), but a fluence dip occurs at later times ($t = 1.6$ to 2.17 ns). This observation is quantified in the radial lineouts shown in Fig. 3, A and C. Although it has been observed in directly driven spherical implosions (*7*), this is the first time such a phenomenon has been measured in x-ray–driven implosions. In these and the earlier experiments, the deflection of proton trajectories is attributed to self-generated radial *E* fields with strength 10^9 to 10^{10} V m^{-1} that are initially directed inward and eventually reverse direction (*7*, *19*). Furthermore, the effects of proton collisional scattering in the shell (which sends some of the protons toward the image center and some away) play a minor role. A number of possible sources of such an *E* field, such as the gradient of plasma electron pressure, acceleration-induced charge separation, and shock-driven plasma polarization, have been proposed to explain the field strength, unique spatial structure, and time evolution (*7*, *19*). This effect will have important implications for ICF implosions; as an example, recent work has demonstrated that such a field leads to a fusion yield anomaly (*20*) through enhanced barodiffusion of different fuel species.

A common feature of the direct-drive implosions is the presence of striations around the capsule or solid CH sphere (*6*). No stochastic filamentary pattern was observed in the fluence images for x-ray–driven implosions, however (Figs. 1 and 2). This result is important for understanding the role of fields in laser and x-ray absorption, instabilities, and thermal transport involved in laser-plasma interactions.

To further characterize the capsule implosion history, quantitative information at different times is extracted from the radial lineouts through the centers of each of the individual images in Fig. 1C. The radial profiles of the mean proton energy (Fig. 3, B and D) [a function of the spatially resolved proton energy loss (*7*, *21*)] are used to infer the capsule ρR, as shown in Fig. 3B, for $t = 0.85$ ns (~2.5 mg cm^{-2}) and Fig. 3D, $t = 2.17$ ns (~8 mg cm^{-2}), indicating more energy loss at a later time due to greater compressions.

In summary, backlighting protons provided the direct observations of spontaneously generated fields and plasma flow, and quantitative characterizations of capsule implosions. The identification of strong (~10^8 to 10^{10} V m^{-1}), local *E* fields and their evolution substantially advance our understanding of both x-ray drive and capsule implosions, and provide critical benchmarks for model validation. Although it provides unique information, this method can be limited sometimes by the directional proton flux and experimental configuration (*22*).

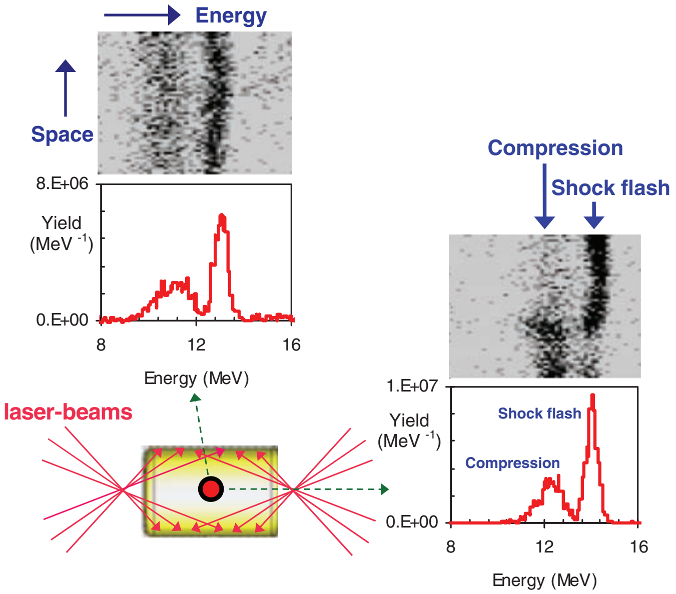

Fig. 4. The spectra and images of self-emitted protons generated from the fusion reaction of D and ^{3}He in an x-ray–driven ICF implosion (OMEGA shot 54744), measured simultaneously at two different directions. The proton yields associated with shock-coalescence burn [the narrow high-energy peak (data bang, in image)] and compression burn [the broad low-energy peak (data bang)] are clearly measured by the energy spectra and spectrally selected images. It is shown that in the direction along LEH, the spatial structure of proton flux is nonuniform (compared with the image along the equator) at both shock flash and compression burn times, with opposing distribution.

To complement the backlighting approach and give further insight into x-ray drive and implosion dynamics and fields, information that cannot be obtained through external backlighting, high-resolution spectrometry of self-emitted charged particles from imploded capsules (*11*) was used. Several important physical quantities, such as ρR at nuclear burn time, fusion yields, and fields around the LEH axis, can be accurately measured through proton self-emission (*22*). As shown in Fig. 4, 14.7-MeV D^{3}He protons generated during the implosion escape the shell and provide information for characterizing implosion performance: first, the charged-particle yield—a fundamental experimental complement to traditional neutron yields; second, measured proton energy loss, which gives information about target areal density [$\rho R = \int \rho (d\varepsilon/dx)^{-1}\, d\varepsilon$] (*21*); and third, measurements of ρR at different angles to quantify implosion asymmetries (*2*, *3*). These measurements can be used to infer a number of important time-dependent implosion phenomena and parameters, such as fuel-shell mix (*2*, *3*), ion and electron temperatures, convergence ratio [$C_r = Q(\rho R/\rho R_0)^{1/2}$, where Q is a function of mass ablation], and spatially resolved capsule structure (*2*, *3*).

In these experiments, the cylindrical vacuum Au hohlraum was 2.45 mm long, with a 1.6-mm diameter and 50% LEH. The 647-μm diameter CH capsule had a shell thickness of 48.2 μm and was filled with 50 atm of D^{3}He (at equal number densities) gas. The hohlraum was driven by 40 beams with total laser energy of 19.7 kJ in a 1-ns square pulse.

Figure 4 shows data collected from D^{3}He protons produced during the nuclear burn: self-emission, spectrally resolved one-dimensional images and energy spectra. The narrow high-energy peak in each spectrum is associated with shock-flash burn (*23*), and the broad low-energy peak with compression burn. After correcting the proton spectrum seen at the equator for the measured energy loss through the 30-μm hohlraum wall, the two peaks are found to have the same energies as those seen through the LEH. Values of ρR inferred from the measured proton energy losses due to passage through the capsule shell indicate that ~20 mg cm^{-2} is achieved at shock flash time and ~80 mg cm^{-2} at the compression burn time in both the polar (toward LEH) and the equatorial directions.

Whereas the proton fluence in the direction of the equator is spatially uniform, the fluence in the LEH direction shows nonuniformities that are different for the two energy components (Fig. 4). Because they are generated at different times (separated by about ~200 ps between the shock flash and compression burn), the nonuniformities have significantly evolved over this time interval. This distribution is not likely to have been caused by proton collisional scattering off the plasmas, because the measured proton energies along both LEH and the equator are very similar. This suggests that the proton fluence nonuniformity is due to self-generated B or E fields near the LEH that do not cause proton energy loss but deflect their trajectories. As shock-flash protons selected by detector have probed a different line-of-sight than the different compression-generated protons, they might see different static small-scale fields. The strength of this B field is estimated to be ~2.5 × 10^5 Tesla-μm. The scale length (the radius of the laser spot) is about 500 μm, suggesting that the B field is about 500 Tesla (5 megaGauss). If the nonuniformities are due to the E field, the strength required (~5 × 10^{10} V m^{-1}) is about one-tenth of the Bohr field, a fundamental field strength for stripping bound electrons, which effectively enhances and sustains the ionizations after lasers are turned off. This value is about a factor of 10 larger than the strength estimated from Faraday's law ($\partial \mathbf{B}/\partial t = -\nabla \times \mathbf{E}$), based on the above-estimated B field strength and 200-ps time scale, suggesting that the time scale for field variation should be ~10 times as fast. The high fields are likely generated in the region near the LEH where the outward-directed axial plasma becomes increasingly resistive after the laser drive ends, leading to the generation, growth, and saturation of low-mode number magneto-instabilities (*24*). The data suggest that the spatial structure or the directions of such fields undergoes rapid changes between the time of shock flash and compression burn.

We thus have a picture in which radiography-generated data show strong fields with a very well-defined fivefold symmetry between the capsule and the hohlraum walls, as well as an axially symmetric radial field inside the capsule. We also have completely complementary data from self-emission imaging showing a strong, rapidly changing, asymmetric field structure near the hohlraum axis.

References and Notes

1. J. Nuckolls, L. Wood, A. Thiessen, G. Zimmerman, *Nature* **239**, 139 (1972).
2. J. Lindl, *Inertial Confinement Fusion* (Springer, New York, 1999).
3. S. Atzeni, J. Meyer-Ter-Vehn, *The Physics of Inertial Fusion* (Claredon, Oxford, 2004).
4. B. A. Remington, D. Annett, R. P. Drake, H. Takabe, *Science* **284**, 1488 (1999).
5. R. P. Drake, *High-Energy-Density Physics* (Springer, New York, 2006).
6. J. R. Rygg *et al.*, *Science* **319**, 1223 (2008).
7. C. K. Li *et al.*, *Phys. Rev. Lett.* **100**, 225001 (2008).
8. R. D. Petrasso *et al.*, *Phys. Rev. Lett.* **103**, 085001 (2009).
9. C. K. Li *et al.*, *Phys. Rev. Lett.* **102**, 205001 (2009).
10. C. K. Li *et al.*, *Phys. Rev. Lett.* **97**, 135003 (2006).
11. F. H. Séguin *et al.*, *Rev. Sci. Instrum.* **74**, 975 (2003).
12. S. I. Braginskii, *Review of Plasma Physics 1* (Consultants Bureau, New York, 1965).
13. M. G. Haines, *Phys. Rev. Lett.* **78**, 254 (1997).
14. J. M. Soures *et al.*, *Phys. Plasmas* **3**, 2108 (1996).
15. D. D. Meyerhofer *et al.*, *Phys. Plasmas* **8**, 2251 (2001).
16. A slight upshift from its birth energy is caused by positive charging of the backlighter target.
17. J. D. Jackson, *Classical Electrodynamics* (Wiley, New York, 1975).
18. The measured width (FWHM) in Fig. 1B is Δ_{15} ~ 260 μm (t = 0.85 ns), which includes both the width W of the jet itself and the spreading δ_{15} of the 15-MeV protons: $\Delta_{15}{}^2 = W^2 + \delta_{15}{}^2$. Because $\delta_3 = (15/3)\ \delta_{15} = 5\ \delta_{15}$, $\Delta_3 \approx 2\ \Delta_{15}$ and $\Delta_3{}^2 = W^2 + \delta_3{}^2$, it follows that $\delta_{15} \approx 90$ μm. Taking the plasma scale length (laser spot size on the wall) L ~ 1.2 mm, the scattering angle in radians can be estimated as ~ $0.5\delta_{15}/L \approx 0.037$. This amount of spreading can be shown to require about $\rho L \approx \rho L_{rad}\ (pv/15\mathrm{MeV})^2 \langle\theta\rangle^2$ ~ 33 mg cm^{-2} of Au, where pv = 30 MeV and ρL_{rad} ~ 6 × 10^3 mg cm^{-2} for Au (*25*). If the five-spoke structure in the images is caused primarily by proton collisional scattering in the spokes, this amount of ρL would lead to ~1 MeV energy loss for 15-MeV protons, which is substantially more than observed in Fig. 1C [energy loss consistent with collisional scattering if we assume that CH in the spoke would be even greater (≈15 MeV)].
19. P. A. Amendt *et al.*, *Plasma Phys. Contr. Fusion* **51**, 124048 (2009).
20. J. R. Rygg *et al.*, *Phys. Plasmas* **13**, 052702 (2006).
21. C. K. Li, R. D. Petrasso, *Phys. Rev. Lett.* **70**, 3059 (1993).
22. The backlighting proton fluence is reduced or even blocked along the hohlraum axis due to the deflection

and/or collisional scattering in the compressed capsule core (Figs. 1 to 3).
23. R. D. Petrasso *et al.*, *Phys. Rev. Lett.* **90**, 095002 (2003).
24. C. K. Li *et al.*, *Phys. Rev. E* **80**, 016407 (2009).
25. T. A. Lasinski *et al.*, *Rev. Mod. Phys.* **45**, S1 (1973).
26. J. J. MacFarlane, *J. Quant. Spectrosc. Radiat. Transf.* **81**, 287 (2003).

27. This work was supported in part by the U.S. Department of Energy and the Laboratory for Laser Energetics (LLE) National Laser User's Facility (DE-FG52-07NA28059 and DE-FG03-03SF22691), Lawrence Livermore National Laboratory (B543881 and LDRD-ER-898988), CEA/DIF (France, Cooperative agreement DE-FC52-08NA28302), LLE (414090-G), Fusion Science Center at University of Rochester (412761-G), and General Atomics (DE-AC52-06NA27279).

9 December 2009; accepted 15 January 2010
Published online 28 January 2010;
10.1126/science.1185747
Include this information when citing this paper.

Deglacial Meltwater Pulse 1B and Younger Dryas Sea Levels Revisited with Boreholes at Tahiti

Edouard Bard,* Bruno Hamelin, Doriane Delanghe-Sabatier

Reconstructing sea-level changes during the last deglaciation provides a way of understanding the ice dynamics that can perturb large continental ice sheets. The resolution of the few sea-level records covering the critical time interval between 14,000 and 9,000 calendar years before the present is still insufficient to draw conclusions about sea-level changes associated with the Younger Dryas cold event and the meltwater pulse 1B (MWP-1B). We used the uranium-thorium method to date shallow-living corals from three new cores drilled onshore in the Tahiti barrier reef. No significant discontinuity can be detected in the sea-level rise during the MWP-1B period. The new Tahiti sea-level record shows that the sea-level rise slowed down during the Younger Dryas before accelerating again during the Holocene.

Understanding the behavior and predicting the fate of large ice sheets can be done in parallel by studying recent and ongoing changes in the climate system (*1*, *2*) and by studying the dramatic sea-level changes that occurred during the last deglaciation [21,000 to 5000 years before the present (yr B.P.)]. To date, the most complete record of deglacial sea level is based on reef cores drilled at Barbados, which have yielded ages from both ^{14}C (*3*–*5*) and mass spectrometric U-Th methods (*5*–*8*). The Barbados record is characterized by two periods of sea-level acceleration [meltwater pulses (MWP) 1A and 1B] that occurred around 14,000 calendar yr B.P. (cal yr B.P.) and 11,300 cal yr B.P., respectively. During each MWP event, the sea level apparently rose by several meters per century, leading to a major hydrological perturbation that probably impacted the ocean circulation [e.g., (*9*, *10*)]. Both the amplitude and the localization of injection into the ocean are crucial in understanding the climatic impact of a MWP event [e.g., (*11*)]. However, several first-order questions remain unresolved on the precise characterization of these events, despite the intensive research carried out over the last decade (see SOM text 1).

The precise timing and amplitude of MWP-1A and 1B are still open questions, because both of these events were originally detected as hiatuses between individual drill cores collected at different depths off Barbados (see SOM text 2 and map in fig. S2). Several other records have been interpreted later as direct or indirect evidence of the occurrence of MWP-1A (*12*–*16*). One of the main goals of the recent Integrated Ocean Drilling Program (IODP) Leg 310 at Tahiti was specifically to collect an additional coral record over the MWP-1A time window. The new suite of coral samples collected during this IODP campaign successfully confirms the existence of MWP-1A and leads to a reassessment of its age and amplitude (*17*).

However, MWP-1B is even more controversial and still needs to be confirmed, both at Barbados and at other far-field sites. Indeed, subsequent coral studies at Huon Peninsula (*18*) and Tahiti (*12*) questioned the timing and amplitude of this freshwater pulse. Additional doubts were also raised about the existence of MWP-1B by a study of sea level in northwest Scotland based on the so-called "marginal basin isolation" technique (*19*). However, the interpretation of this Scottish record is complex due to its proximity to former ice sheets in a region where the postglacial rebound contribution is dominant, which explains why the local sea level continued to fall during most of the deglaciation. So far, the sample coverage and depth resolution of these different studies are still insufficient to reach a definitive conclusion about MWP-1B. Unfortunately, the new IODP sample collection from Tahiti is of little help in studying MWP-1B, because the depth range of the drill cores was targeted on MWP1-A and the earliest part of the deglaciation (i.e., 90 to 120 m). At these depths, only deep-living coral species persisted in the reef at the levels corresponding to the age of MWP-1B.

To settle the issue, we dated by U-Th 47 pristine coral samples from three new reef cores (P8, P9, and P10) drilled onshore of the Papeete barrier reef in Tahiti, close to the location of our previous study (23 U-Th dated corals from P6 and P7 cores) (*12*). P8 is at about the same position as P7 (*12*) but was drilled at an angle of 33° toward the sea, whereas P9 and P10 were collected in the inner part of the barrier reef toward the Papeete Pass (fig. S1).

Figure 1B shows a comparison of the new U-Th data from P8, P9, and P10 cores with the previous Tahiti record (*12*). Unlike the Barbados cores, each of these Tahiti cores yields an uninterrupted record of the time window corresponding to MWP-1B. The new U-Th data (Fig. 1B and table S1) provide an unprecedented resolution and can be compared to the other sea-level records from Barbados (*7*, *8*), Papua New Guinea (Huon Peninsula) (*18*, *20*), and Vanuatu (Urelapa) (*21*) (Fig. 1, C and D). The North Greenland Ice Core Project (NorthGRIP) isotope record is also plotted in Fig. 1A using its most recent time scale (*22*). This is done to compare the sea-level records with climatic transitions such as the inception and the end of the Younger Dryas (YD), which marks the start of the Holocene period.

The large number of data points derived from the four cores provides a very accurate constraint on the sea-level rise during this period, defined by the coherent upper envelope of the paleo-depths of the samples. The small scatter of the data reflects the inherent uncertainty linked to the paleo-bathymetry of corals and associated shallow-living biological assemblages (*23*, *24*). Part of this overall scatter is also related to the different positions of the drill cores on the barrier reef (SOM text 2 and fig. S1). P9 and P10 record the upper reef crest on the inner part of the barrier. By contrast, P8 was drilled on the outer part of the barrier reef, with a deviation of 33° toward the sea. Therefore, in the lower sections of P8 below 65 m, the corals (red points in Fig. 1B) plot slightly lower than those from P7, P9, and P10, a difference that remains small (<6 m) but fairly systematic.

The rate of sea-level rise at Tahiti can be calculated by means of linear fits over the three specific climatic intervals: before, during, and after the YD event (thick lines in Fig. 1B) (see SOM text 2 and table S2 for details). Taken together, the Tahiti data define a relatively smooth sea-level rise, with no significant acceleration during the time interval corresponding to

---

Centre Européen de Recherche et d'Enseignement des Géosciences de l'Environnement (CEREGE), UMR 6635 CNRS, University Aix-Marseille, Institut de Recherche pour le Développement, Collège de France, Europôle de l'Arbois, BP 80, F-13545 Aix-en-Provence Cedex 4, France.

*To whom correspondence should be addressed. E-mail: bard@cerege.fr